



HAL
open science

Coupled natural convection and radiation in a cubic cavity filled with an air - H₂O mixture in the presence of a heated obstacle

Xuan Bach Nguyen, Didier Saury, Denis Lemonnier

► **To cite this version:**

Xuan Bach Nguyen, Didier Saury, Denis Lemonnier. Coupled natural convection and radiation in a cubic cavity filled with an air - H₂O mixture in the presence of a heated obstacle. *Progress in Computational Fluid Dynamics*, 2022, 22 (3), pp.131-138. 10.1504/PCFD.2022.123181 . hal-03707005

HAL Id: hal-03707005

<https://cnrs.hal.science/hal-03707005>

Submitted on 22 Dec 2023

HAL is a multi-disciplinary open access archive for the deposit and dissemination of scientific research documents, whether they are published or not. The documents may come from teaching and research institutions in France or abroad, or from public or private research centers.

L'archive ouverte pluridisciplinaire **HAL**, est destinée au dépôt et à la diffusion de documents scientifiques de niveau recherche, publiés ou non, émanant des établissements d'enseignement et de recherche français ou étrangers, des laboratoires publics ou privés.

[cite as:](#)

X. B. Nguyen, D. Saury, D. Lemonnier, « Coupled natural convection and radiation in a cubic cavity filled with an air-H₂O mixture in the presence of a heated obstacle », *Progress in Computational Fluid Dynamics*, Volume 22(3) pp. 139–158, 2022. DOI: 10.1504/PCFD.2021.10042895

1

Coupled natural convection and radiation in a cubic cavity filled with an *air* – *H₂O* mixture in the presence of a heated obstacle

Xuan Bach NGUYEN

E-mail: xuan-bach.nguyen@ensma.fr

Didier SAURY

E-mail: didier.saury@ensma.fr

Denis LEMONNIER

E-mail: denis.lemonnier@ensma.fr

Abstract: Natural convection in a cubical cavity with a hot obstacle located on its floor is investigated. The inner fluid is a semi-transparent mixture of dry air and water vapor, which creates a coupled convective and radiative transport within the fluid. The conservation equations are solved by a finite volume method and the radiative transfer equation by using the discrete ordinates method. The radiative properties of the mixture are accounted for by a spectral line weighted sum of gray gases model associated to the rank correlated approach. It was observed that the volume radiation has a strong influence on the thermal and dynamic fields. The nearly vertical stratification of the temperature field around the plume is broken. Radiation also accelerates the boundary layers near the lateral surfaces and the ceiling and the floor of the enclosure. The total heat transfer is decreased due to both the reduction in convective process near the vertical walls and the attenuation by radiation.

Keywords: Heat transfer, Convection, Radiation, Numerical method

1 Introduction

The study of natural convection in confined environments is still the subject of many research, both numerically and experimentally. In this type of problem, the different modes of heat transfer (convection, conduction, radiation) can intervene in a coupled way. However, when radiative transport is considered, a particular problem arises when the fluid behaves as a semi-transparent medium, i.e., absorbs and emits infrared radiation. It is then necessary to take into account an internal heat source within the medium, resulting from

the difference between the radiant energy absorbed and emitted by each volume element. Many studies have investigated this phenomenon in a rectangular enclosure (Yücel et al. (1989), Tan and Howell (1991), Colomer et al. (2004a), Colomer et al. (2007), Soucasse et al. (2012), Billaud et al. (2017), Hajji et al. (2018)). The problem of a heat supply placed in a confined environment has also received attention, either with point source (Tetsu et al. (1973), Urakawa et al. (1983), Xin et al. (2004), Hernandez (2015), etc.) or with finite sized solid obstacles (Kuznetsov and Sheremet (2006a), Kuznetsov and Sheremet (2006b), Xu and Wang (2008), Paroncini and Corvaro (2009), Kuznetsov et al. (2013), Souayeh et al. (2015), Gibanov and Sheremet (2016), Iyi et al. (2013) Rahmati and Tahery (2018), etc.), but in most cases the heat source is set within the fluid, without any contact with the walls. Here, we address the case of a heating obstacle placed on the floor of the cavity. This constitutes a new worthy configuration of interest.

First of all, concerning the natural convection inside a cavity containing an opaque obstacle, Kuznetsov and Sheremet (2006b) have investigated the effects of the Grasshof number ($10^5 - 10^7$) on the fluid motion and concluded the influence of this parameter on the thermal field in the enclosure. Kuznetsov and Sheremet (2006a) have studied the same configuration, but with a different range of the Grasshof number ($10^7 - 10^9$) and pointed out that as this number increases, the flow and the heat transfer process are stabilized. Paroncini and Corvaro (2009), Kuznetsov et al. (2013) Souayeh et al. (2015), Gibanov and Sheremet (2016), Iyi et al. (2013) Rahmati and Tahery (2018) have studied different convective flow in both numerical and experimental manners with the influence of the Rayleigh number. They have reported that the increase of this parameter intensifies the fluid motion and raises the heat transfer through convective process. In addition, the study on the hot obstacle size of Paroncini and Corvaro (2009) pointed out that, when the height of the obstacle is a half of the cavity, the convective heat transfer is the worst among the analyzed cases. Besides, Bouafia and Daube (2007) have considered the unsteady behaviors in this configuration at different aspect ratio of the enclosure and concluded that the mechanism of the unsteadiness was the shear instabilities when the aspect ratio is 1 and 2. For higher aspect ratio (4), the leading mechanism was the buoyancy instabilities. Hernandez (2015) has studied a square cavity with a heat source attached to the floor. His results point out that the unsteady behavior was due to the high horizontal velocity right above the obstacle.

Next, the problem of natural convection combined with the surface radiation have been investigated by Sun et al. (2011), Martyushev and Sheremet (2013), Saravanan and Sivaraj (2014), Patil et al. (2016), Miroshnichenko et al. (2018). They have concluded that the increase in the emissivity strengthens the fluid motion near the wall, intensifies the radiative transfer but reduces the convective transport. Sun et al. (2011) have also reported that surface radiation slows down the transition to the unsteadiness inside the cavity.

Through a detailed literature review, it is shown the lack of observations on the flow characteristics when the medium is filled by a radiatively participating gas mixture in the configuration of a cavity with a heat source inside. This work, therefore, addresses this problem by numerical simulations of the coupling natural convection and gas radiation in a cubical enclosure filled with an *air* – H_2O mixture and a heated obstacle located on its floor.

Nomenclature

Physical symbols

g	gravitational acceleration	$9.81 \text{ m} \cdot \text{s}^{-2}$
n	unit normal vector	
q_r	radiative flux vector	$W \cdot \text{m}^2$
s	a point on a propagation direction of radiation	
ΔT	temperature difference	K
A	area of considered surface	m^2
a_j	weight of j^{th} gray gas	
C	absorption cross section	$\text{m}^2 \cdot \text{mol}^{-1}$
G	incident radiation	$W \cdot \text{m}^{-2}$
I	radiative intensity	$W \cdot \text{m}^{-2} \cdot \text{sr}$
L	cavity length	m
l	obstacle size	m
N_g	number of gray gases	
P	absolute pressure	Pa
q^{inc}	incident radiative flux	$W \cdot \text{m}^{-2}$
q^{net}	net radiative flux, $q^{net} = \sigma T_w^4 - q^{inc}$	$W \cdot \text{m}^{-2}$
R	ideal gas constant	$8.3144621 \text{ J} \cdot \text{K}^{-1} \cdot \text{mol}$
t	time	s
T_c	absolute temperature at cold surfaces	K
T_h	absolute temperature at hot surfaces	K
T_w	absolute wall temperature	K
T_{ref}	reference temperature, $T_{ref} = (T_h + T_c)/2$	K
u, v, w	velocity component	$\text{m} \cdot \text{s}^{-1}$
U_x	normalized velocity component, $U_x = \frac{u}{U_{ref}}$	
U_{ref}	reference velocity, $U_{ref} = \alpha \frac{\sqrt{Ra}}{L}$	$\text{m} \cdot \text{s}^{-1}$
X, Y, Z	normalized coordinates, $X = \frac{x}{L}, Y = \frac{y}{L}, Z = \frac{z}{L}$	
x, y, z	Cartesian coordinates	m

4

x_{H_2O} molar fraction of H_2O in the mixture

Dimensionless numbers

Nu_c convective Nusselt number, $Nu_c = \frac{L}{\Delta T} \left| \frac{\partial T}{\partial x} \right|$

Nu_r radiative Nusselt number, $Nu_r = \frac{L|q^{net}|}{\lambda \Delta T}$

Nu_t total Nusselt number, $Nu_t = Nu_c + Nu_r$

Pl Planck number, $Pl = \frac{\lambda L}{4\sigma T_{ref}^3}$

Pr Prandtl number, $Pr = \frac{\nu}{\alpha}$

Ra Rayleigh number, $Ra = \frac{g\beta_T \Delta T L^3}{\alpha \nu}$

Greek symbols

α thermal diffusivity $m^2 \cdot s^{-1}$

β_T thermal expansion coefficient K^{-1}

ϵ emissivity

η wavenumber cm^{-1}

κ absorption coefficient m^{-1}

λ thermal conductivity $W \cdot m^{-1} \cdot K^{-1}$

ν kinematic viscosity $m^2 \cdot s^{-1}$

Ω solid angle sr

Ω_m discrete direction

ρ density $kg \cdot m^{-3}$

σ Stefan Boltzmann constant $5.670367 \times 10^{-8} W \cdot m^{-2} \cdot K^{-4}$

Abbreviation

ALBDF Absorption Line Blackbody Distribution Function

2 Mathematical model

2.1 Problem statement

The configuration under consideration in this research is illustrated in figure 1. It deals with a cubical cavity of size $L = 0.25m$ having adiabatic horizontal walls, while the vertical ones are maintained at a constant and uniform temperature (T_c). A small solid cube of size $l = 0.05m$ is located at the center of the bottom wall. It creates an opaque obstacle whose surfaces are uniformly set at a higher temperature ($T_h > T_c$).

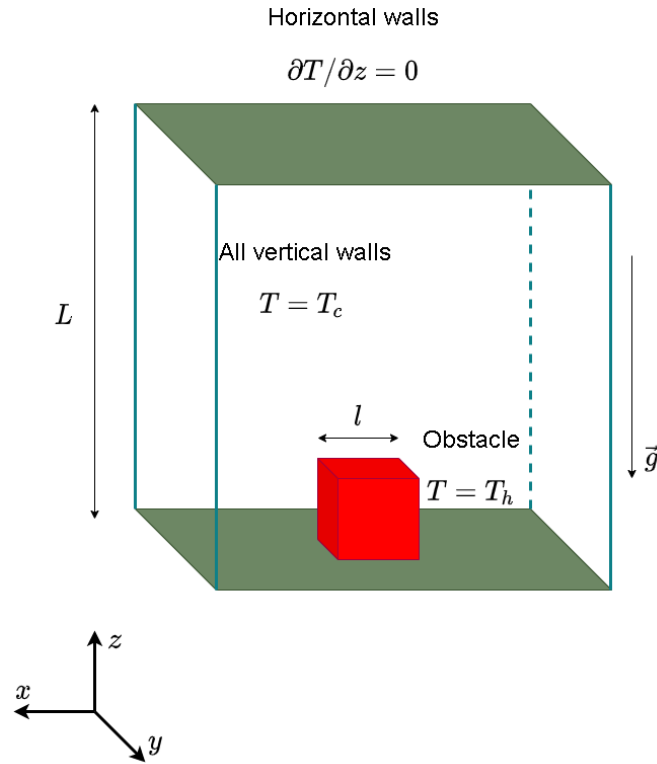


Figure 1 Configuration of the calculation

The enclosure is filled with either dry air or a mixture of air and water vapor, depending on the case study. The medium is homogeneous in composition. The temperature difference between the obstacle and the cavity generates a natural convection flow and, when water vapor is present, H_2O acts as an emitting-absorbing component for infrared radiation.

2.2 Conservation equations

Several conservation equations govern the flow motion and the transfer processes in the enclosure. They express a local balance in mass, momentum, energy and composition within the fluid:

- Continuity equation

If density variations are neglected, the total mass conservation reads:

$$\nabla \cdot \mathbf{u} = 0 \quad (1)$$

- Momentum equation

$$\rho_0 \frac{\partial \mathbf{u}}{\partial t} + \rho_0 \mathbf{u} \cdot \nabla \mathbf{u} = -\nabla p + \rho_0 \beta_T (T_0 - T) \mathbf{g} + \mu \nabla^2 \mathbf{u} \quad (2)$$

The source term $\rho_0\beta_T(T_0 - T)\mathbf{g}$ accounts for the buoyancy force that sets the fluid into motion (here expressed under the Boussinesq approximation).

- Energy equation

$$\rho_0 C_p \frac{\partial T}{\partial t} + \rho_0 C_p \mathbf{u} \cdot \nabla T = \lambda \nabla^2 T - \nabla \cdot \mathbf{q} \quad (3)$$

The divergence term $-\nabla \cdot \mathbf{q}$ is the internal radiative source resulting from the difference between the absorbed and emitted radiant energy in each elementary volume of fluid. It takes non-zero values whenever H_2O is present in the mixture.

2.3 Radiative transfer equation

The spectral radiative intensity $I_\eta(\mathbf{s}, \boldsymbol{\Omega})$ represents the radiant flux (per unit angle solid and per unit wavenumber) that propagates at point $\mathbf{s} = (x, y, z)$ in the direction $\boldsymbol{\Omega}$ at the wavenumber η . The local change of intensity is described by the radiative transfer equation, which, for a non-scattering medium, is expressed as:

$$\boldsymbol{\Omega} \cdot \nabla I_\eta(\mathbf{s}, \boldsymbol{\Omega}) = -\kappa_\eta(\mathbf{s}) I_\eta(\mathbf{s}, \boldsymbol{\Omega}) + \kappa_\eta(\mathbf{s}) I_{b\eta}(T(\mathbf{s})) \quad (4)$$

where $\kappa_\eta(\mathbf{s})$ is the local spectral absorption coefficient defined as $\kappa_\eta(\mathbf{s}) = N(\mathbf{s}) Y(\mathbf{s}) C_\eta(\phi(\mathbf{s}))$. In this expression, $C_\eta(\phi(\mathbf{s}))$ is the spectral absorption cross section, depending on the local thermodynamic state, $\phi(T, P, C)$, $Y(\mathbf{s})$ the mole fraction and $N(\mathbf{s})$ the molar density of the absorbing species (Denison and Webb (1993)). The radiative intensity depends on three position coordinates, two direction variables (either two polar angles or two direction cosines) and the wavenumber. The total intensity can be found by integration over the whole spectrum as:

$$I(\mathbf{s}, \boldsymbol{\Omega}) = \int_0^\infty I_\eta(\mathbf{s}, \boldsymbol{\Omega}) d\eta \quad (5)$$

The source term $-\nabla \cdot \mathbf{q}$, which appears in the energy equation, is the total divergence of the radiative flux. This flux can be calculated from the total intensity by the expression:

$$\mathbf{q}(\mathbf{s}) = \int_0^{4\pi} I(\mathbf{s}, \boldsymbol{\Omega}) \boldsymbol{\Omega} d\Omega = \int_0^{4\pi} \int_0^\infty I_\eta(\mathbf{s}, \boldsymbol{\Omega}) \boldsymbol{\Omega} d\eta d\Omega \quad (6)$$

and, as a result (Modest (2013)):

$$-\nabla \cdot \mathbf{q}(\mathbf{s}) = \int_0^\infty \int_0^{4\pi} \kappa_\eta(\mathbf{s}) I_\eta(\mathbf{s}, \boldsymbol{\Omega}) d\Omega d\eta - 4\pi \int_0^\infty \kappa_\eta(\mathbf{s}) I_{b\eta}(T(\mathbf{s})) d\eta \quad (7)$$

2.4 Spectral model

When gas radiation is considered, the actual spectral behavior of the fluid (absorption) must be accounted for. In this work, the Spectral Line-based Weighted-sum-of-gray-gases models (SLW) (Denison and Webb (1993)) has been selected. This model, according to Goutiere et al. (2000) and Goutière et al. (2002), provides the best compromise between accuracy and computational cost.

The SLW model involves a finite number (N_g) of gray gases and one clear (transparent) gas. The absorption coefficient of j^{th} gas is calculated as:

$$\kappa_j = N \cdot Y \cdot C_j \quad (8)$$

where C_j is the absorption cross section. Knowing N and Y , the remaining problem is to determine C_j . This parameter is here determined as $C_j = \sqrt{\tilde{C}_{j-1}\tilde{C}_j}$ where $\tilde{C}_j = C_{min}(C_{max}/C_{min})^{j/N_g}$ is the supplemental cross section selected in the range $[C_{min}, C_{max}]$.

The weight of the j^{th} gray gas a_j corresponds to the difference in the absorption line black body distribution function ALBDF at the two supplemental absorption cross sections that define the j^{th} interval $[\tilde{C}_{j-1}, \tilde{C}_j]$ (Denison and Webb (1994)):

$$\begin{aligned} a_j &= F(\tilde{C}_j, \phi_g, T_b) - F(\tilde{C}_{j-1}, \phi_g, T_b) : \text{for } j = 1, \dots, N_g \\ a_0 &= F(\tilde{C}_0, \phi_g, T_b) \end{aligned} \quad (9)$$

where T_b is equal to the local temperature in the fluid and to the wall temperature at the boundaries.

The ALBDF is evaluated as the integral of the Planck function calculated at a source temperature T_b over the wavenumber intervals such that the absorption cross section $C_\eta(\phi_g)$ at a gas thermodynamic state ϕ_g is below a prescribed C-value, namely:

$$\begin{aligned} F(C, \phi_g, T_b) &= \frac{1}{E_b(T_b)} \int_{\eta: C_\eta(\phi_g) < C} E_{b\eta}(T_b) d\eta \\ &= \frac{\pi}{\sigma T_b^4} \int_{\eta: C_\eta(\phi_g) < C} I_{b\eta}(T_b) d\eta \end{aligned} \quad (10)$$

The ALBDF is determined by performing integrations over the whole spectrum at high resolution (line by line) and different pressures, temperatures and compositions. The resulting data are made available for the main participating species (H_2O , CO_2 , CO) either as mathematical correlations or in look-up tables. The most recent contribution is reported in Pearson et al. (2014) and is based on the HITEMP-2000 spectral database. In this research, the look-up tables provided by Solovjov (2014) have been used along with the rank-correlated approach (Solovjov et al. (2017)) to handle the fluid temperature variations.

Finally, the radiative transfer equation for the j^{th} gray gas is written as :

$$\boldsymbol{\Omega} \cdot \nabla I_j(\mathbf{s}) = -\kappa_j I_j(\mathbf{s}) + a_j \kappa_j I_b(\mathbf{s}) \quad (11)$$

The total intensity and radiative source term are then obtained by the following expressions:

$$I(\mathbf{s}, (\boldsymbol{\Omega})) = \sum_{j=1}^{N_g} I_j(\mathbf{s}, (\boldsymbol{\Omega})) \quad (12)$$

$$\nabla \cdot \mathbf{q}(\mathbf{s}) = \sum_{j=1}^{N_g} (\kappa_j \int_0^{4\pi} G_j(\mathbf{s}) - 4\pi a_j \kappa_j I_b(\mathbf{s})) \quad (13)$$

where $G_j(\mathbf{s}) = \int_0^{4\pi} I_j(\mathbf{s}, \boldsymbol{\Omega}) d\Omega$ is the incident radiation related to the j^{th} gray gas.

2.5 Boundary conditions

Kinematic, mass and thermal fields

All the surfaces of the heated obstacle, except the one in contact with the floor of the cavity, are black and set at constant and uniform temperature:

$$T = T_h, \quad \epsilon = 1 \quad (14)$$

Regarding the cavity:

- Vertical walls are black and uniformly maintained at constant temperature:

$$T = T_c, \quad \epsilon = 1 \quad (15)$$

- Horizontal walls are adiabatic and assumed to behave as fully reflective surfaces:

$$\frac{\partial T}{\partial z} = 0 \quad \text{with } z = 0, L. \quad \epsilon = 0 \quad (16)$$

Zero velocities are applied to all the walls of the cavity and all the surfaces of the obstacle.

Radiative intensity field

Intensity at the bounding walls is prescribed for all directions $\boldsymbol{\Omega}$ pointing inward to the cavity that is for $\boldsymbol{\Omega} \cdot \mathbf{n} > 0$ where \mathbf{n} is the local unit vector. Assuming gray diffuse surfaces, the boundary condition reads:

$$I_\eta(\mathbf{s}, \boldsymbol{\Omega}_{(\boldsymbol{\Omega} \cdot \mathbf{n} > 0)}) = \epsilon I_{b\eta}(T(\mathbf{s})) + (1 - \epsilon) \frac{q_\eta^{inc}}{\pi} \quad (17)$$

where:

$$q_\eta^{inc} = \int_{\boldsymbol{\Omega} \cdot \mathbf{n} < 0} I_\eta(\mathbf{s}, \boldsymbol{\Omega}) |\boldsymbol{\Omega} \cdot \mathbf{n}| d\Omega \quad (18)$$

In this study, the surfaces of the obstacle and the vertical walls of the cavity are black ($\epsilon = 1$) and the horizontal walls of the enclosure are purely reflective ($\epsilon = 0$).

3 Methodology

All the governing equations of our problem were solved by using Code Saturne-version 5.0.4 (Archambeau et al. (2004)), an open source software for CFD calculation developed by EDF. A built-in radiative module is available, in which we have implemented our own data for directional integration and a specific module for gas radiation according to the SLW model.

3.1 Computational Fluid Dynamics

Code Saturne uses a finite volume method to solve the governing equations of fluid motion and heat and mass transfer. For the momentum equations, Code Saturne resorts to the SIMPLEC algorithm (Semi-Implicit Methods for Pressure Linked Equations Consistent). Different discretizations in space and in time are also available.

Temporal discretization

The time scheme is implemented in Code Saturne is a θ – scheme with:

$$\begin{cases} \theta = 1 & \text{for an implicit first order Euler scheme,} \\ \theta = \frac{1}{2} & \text{for second order Crank-Nicolson scheme.} \end{cases} \quad (19)$$

There are two options for setting the temporal step: constant and variable. In the latter case, the code automatically calculates the time step after each iteration that satisfies the CFL criterion. In our study, we have used the implicit first order backward Euler scheme along with the variable time step option.

Spatial discretization

Code Saturne proposes different schemes of first order (Upwind) and second order (Centered or Second-Order-Linear-Upwind (SOLU)) for spatial discretization and. In this study, we have selected the centered second order scheme.

3.2 The Discrete Ordinates Method

The discrete ordinates method (DOM) has been used to solve the radiative transfer equation corresponding to each gray gas of SLW model. This method consists in replacing the angular integrals by a summation over a set of discrete directions such as:

$$\int_0^{4\pi} f(\boldsymbol{\Omega})d\boldsymbol{\Omega} \approx \sum_{m=1}^M \omega_m f(\boldsymbol{\Omega}_m) \quad (20)$$

where M denotes the number of directions in the set and ω_m is the weight attributed to the m^{th} element. Consequently, the distribution of incident radiation and radiative flux are approximated by:

$$G_\eta^P = \int_0^{4\pi} I_\eta^P(\boldsymbol{\Omega})d\boldsymbol{\Omega} \approx \sum_{m=1}^M \omega_m I_{\eta,m}^P(\boldsymbol{\Omega}) \quad (21)$$

$$\mathbf{q}_m^P = \int_0^{4\pi} I_\eta^P(\boldsymbol{\Omega}) \boldsymbol{\Omega} d\boldsymbol{\Omega} \approx \sum_{m=1}^M \omega_m I_{\eta,m}^P(\boldsymbol{\Omega}) \boldsymbol{\Omega}_m \quad (22)$$

where P here denotes the center of a control volume.

There are several ways to define the discrete direction sets. A more general overview on this problem can be found in Koch and Becker (2004). We have here selected the level symmetric S_N quadrature using the improved dataset suggested by Balsara (2001).

3.3 Code Validation

3.3.1 Differentially heated cavity

In this section, Code Saturne and its improved radiative model is validated through the simulations of both pure thermal convection and double diffusive convection coupled with radiation in a differentially heated cavity (see figure 2).

Pure Thermal Convection

In that case, there is no radiative effects (transparent medium, non-emitting walls). The Prandtl number is 0.71 and the computations were run over a uniform grid of 80^2 cells. In this configuration, many references are available (Le Quéré (1991), Tric et al. (2000)...). Here, the solutions are compared against the data provided by De Vahl Davis (1983) and are presented below. A good agreement is found between our results and this reference (see Table 1).

Ra	Our work	De Vahl Davis (1983) (Relative Difference %)
10^3	1.113	1.117 (0.36)
10^4	2.235	2.238 (0.13)
10^5	4.507	4.509 (0.04)
10^6	8.816	8.817 (0.01)

Table 1 Mean Nusselt number on the hot wall

Regarding 3-D cases, we have performed calculations in the configurations studied by Colomer et al. (2004b) and Fusegi and Hyun (1994). A uniform 81^3 grid was used still with $Pr = 0.71$. Here too, a good agreement is observed with the reference data (see Table 2).

Ra	Our work	Colomer et al. (2004b)	Fusegi and Hyun (1994)
10^4	2.059	2.030 (1.42%)	2.100 (1.95 %)
10^5	4.365	4.334 (0.71 %)	4.361 (0.09%)
10^6	8.717	8.862 (1.63%)	8.770 (0.60 %)

Table 2 Mean Nusselt Number on the hot wall (Pr = 0.71)

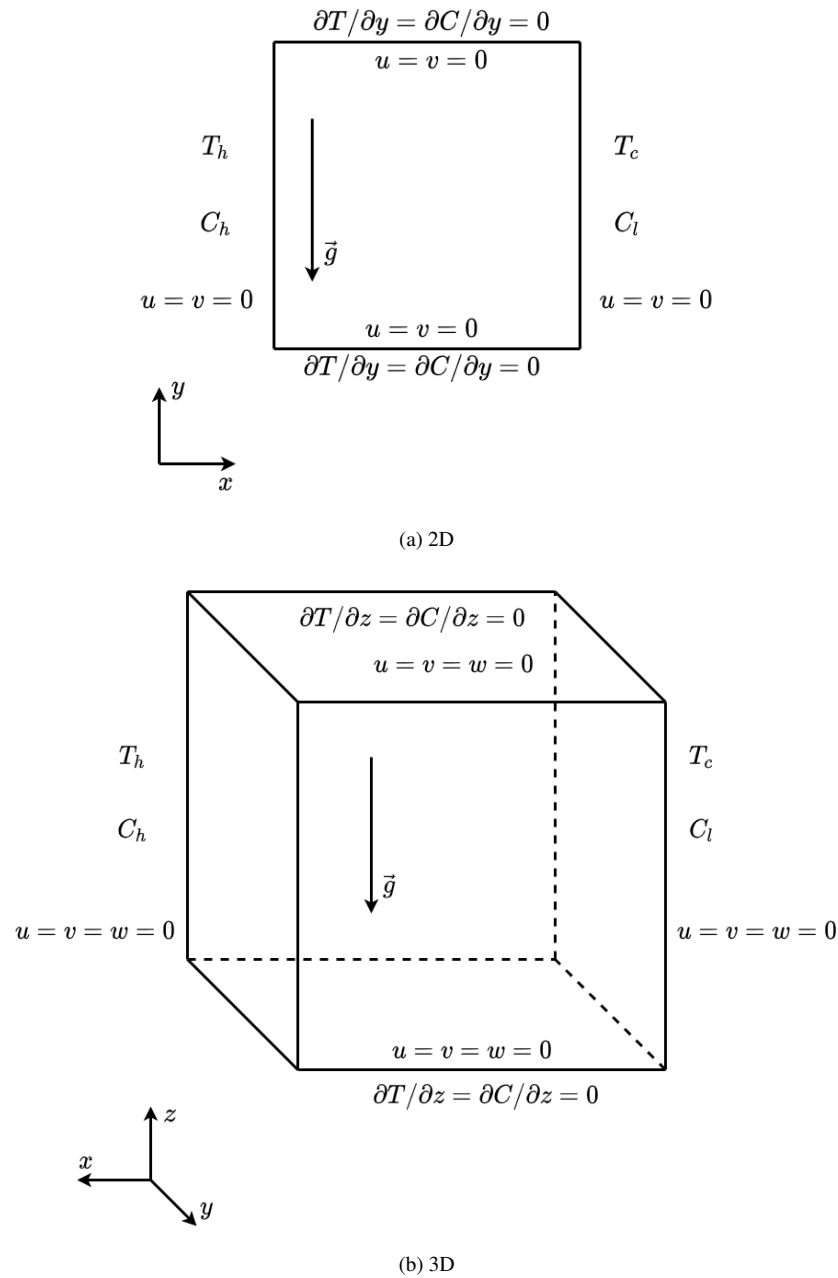


Figure 2 Differentially heated cavity

Pure Thermal Convection coupled with radiation

We now consider a semitransparent fluid (absorbing and emitting in volume). The results of our simulations are compared against data provided by Yücel et al. (1989) (Ref.1) and Laouar-Meftah (2010) (Ref.2) for coupled thermal convection and radiation in a gray gas inside a 2D differentially heated square cavity. In Yücel et al. (1989), the authors have

used a non-uniform 50^2 grid (but they did not specify of which type) and performed the calculations at different values of the overall optical thickness $\tau = \kappa \cdot L$ (L is the cavity size and κ the gray absorption coefficient). The Rayleigh number was fixed at $5 \cdot 10^6$ with $Pr = 0.72$ and the Planck number defined as $Pl = \frac{\lambda}{4\sigma L T_{ref}^3}$ was set to $Pl = 0.02$. All the bounding walls are black and the temperature ratio ($\theta_0 = T_{ref}/\Delta T$) is set to 1.5. A non-uniform 81^2 grid is used, like in reference Laouar-Meftah (2010). The results are listed in Table 3. They show that the difference between our calculations and the reference does not exceed 4 %. This difference may come from different interpolation schemes used in the DOM (the Lathrop variable scheme in Laouar-Meftah (2010), the STEP scheme in the present work).

τ	S_N	Convective Nusselt			Total Nusselt		
		Our work	Ref.1	Ref.2	Our work	Ref.1	Ref.2
0.2	S_4	36.01	37.40	37.40	46.50	46.11	46.05
1	S_8	31.88	31.25	31.25	39.38	38.93	38.81
5	S_4	24.58	23.64	23.57	31.47	31.76	31.59

Table 3 Mean Nusselt number on the hot wall ($Pr = 0.71$, $Pl = 0.02$, $\theta_0 = 1.5$, $\epsilon_i = 1$)

In addition, we have performed different validation tests in a 3-D differentially heated cavity filled with a real participating gas (that is, accounting for the actual absorption spectrum of the medium). We have reproduced the works of Billaud et al. (2017) by considering a cubic enclosure filled with humid air (*air* – H_2O mixture). Different case studies based on the radiative behavior of the bounding walls and the medium have been investigated. They are described in Table 4. Our calculations have been carried out using a non-uniform 91^3 grid like in reference Billaud et al. (2017). Our results are also compared to the data provided by Soucasse et al. (2016) and presented in Table 5. The comparisons show a fairly good agreement between our predictions and the two references.

Case	A	B	C	D
Isothermal walls	$\epsilon = 1$	$\epsilon = 1$	$\epsilon = 1$	$\epsilon = 1$
Adiabatic walls	$\epsilon = 0$	$\epsilon = 0$	$\epsilon = 1$	$\epsilon = 1$
Gas nature	Transparent	Participating	Transparent	Participating

Table 4 Radiative boundary conditions and radiative properties of the medium

Case	Our work	Billaud et al. (2017)	Soucasse et al. (2016)
A	8.64	8.65 (0.11 %)	8.64 (0.0 %)
B	7.24	7.42 (2.42 %)	7.55 (4.10 %)
C	7.93	8.10 (2.09 %)	8.47 (6.37 %)
D	8.48	8.01 (5.86 %)	8.48 (0.0 %)

Table 5 Mean convective Nusselt number on the hot wall (*air* – H_2O mixture, $Ra = 10^6$, $Pr = 0.707$)

3.3.2 Cavity with a hot obstacle

Our purpose is now to test the ability of our simulation code to handle geometries involving obstacles. The first validation test considers a 2-D square cavity with a heat source located at the center of the bottom wall (see figure 3). The enclosure is 0.05m long. The heat source is 0.01 m wide and 0.025 m high. The enclosure is filled by dry air (transparent) and the Prandtl number is set to 0.71. The heat source is maintained at $T_h = 301.16$ K while two lateral walls of the cavity are prescribed at $T_c = 291.16$ K. The remaining surfaces of the enclosure are adiabatic. The tests are performed at different Rayleigh numbers, using a 100^2 uniform grid and the results are compared to the experiments and the simulations of Paroncini and Corvaro (2009).

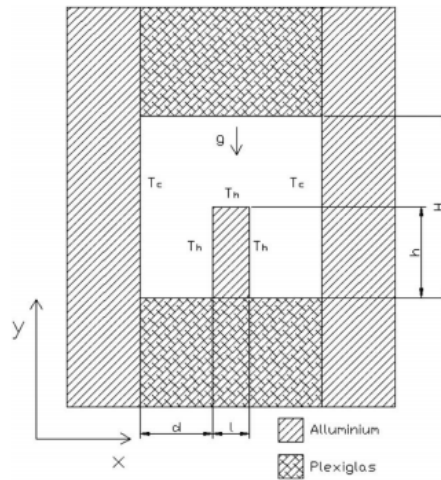


Figure 3 First validation test

Ra	Reference (exp)	Reference (num)	Our work
$1.02 \cdot 10^5$	10.49	10.46	10.42
$1.21 \cdot 10^5$	10.96	10.96	10.96
$1.48 \cdot 10^5$	11.46	11.58	11.61
$1.68 \cdot 10^5$	11.89	11.99	12.04
$1.93 \cdot 10^5$	12.34	12.45	12.52
$2.11 \cdot 10^5$	12.71	12.76	12.84

Table 6 First validation test: Mean Nusselt number on the lateral wall of the heated obstacle. The reference length is the cavity size (H).

The comparisons of our results with the reference show a good agreement, the maximum difference being less than 1 % when comparing the two numerical simulations. Differences are larger with respect to measured quantities (but this is also true in the reference work). Some thermal leakage through the plexiglas plates (imperfect insulation) may explain these

variations.

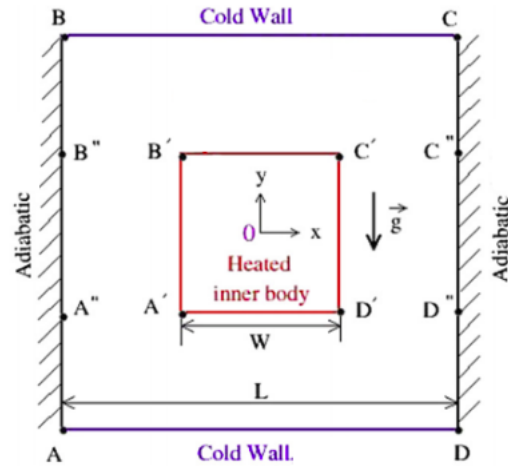


Figure 4 Second validation test

The second validation considers a hot obstacle located at the center of a 2D square cavity (see figure 4). Now, two vertical walls of the cavity are kept adiabatic while the horizontal one are maintained at a constant lower temperature compared to the isothermal heated obstacle. The enclosure is filled with dry air. The simulation is run at a Rayleigh number of $Ra = 2 \cdot 10^5$ and a Prandlt number of $Pr = 0.71$. The comparisons with the results of Sun et al. (2011) reported in table 7 prove that our code can efficiently handle this type of configuration, both for the flow description and thermal transport (the maximum difference is less than 0.5 %).

	Our work	Sun et al. (2011)	Relative difference (%)
Side A'B' or C'D'	3.7129	3.7174	0.121
Side A'D' (bottom)	5.6527	5.6347	0.319
Side B'C' (top)	9.4989	9.4614	0.396
Bottom wall	2.5342	2.5346	0.015
Top Wall	6.4966	6.4778	0.290

Table 7 Second validation test: Mean Nusselt number on different walls ($Ra = 2 \cdot 10^5$, $Pr = 0.71$)

4 Results and Discussion

The enclosure under study is filled with a real *air* – H_2O mixture. It involves an absorbing-emitting component (H_2O) diluted at different concentrations into a transparent gas (dry air). The temperature of the hot obstacle is set to $T_h = 580K$ and the vertical walls of the cavity are maintained at $T_c = 530K$. The thermophysical properties of the mixture are

calculated at the reference temperature according to the perfect gas law for density and the Wilke-Wassiljewa formulas for dynamic viscosity and thermal conductivity, as suggested in Meftah et al. (2009). The actual absorption spectrum is accounted for by using the SLW model.

The characteristic parameters of the simulations are presented in Table 8.

x_{H_2O} (%)	Ra	Pr	PI
5	$4.663 \cdot 10^6$	$7.251 \cdot 10^{-1}$	$4.394 \cdot 10^{-3}$
10	$4.693 \cdot 10^6$	$7.351 \cdot 10^{-1}$	$4.392 \cdot 10^{-3}$
20	$4.753 \cdot 10^6$	$7.553 \cdot 10^{-1}$	$4.389 \cdot 10^{-3}$

Table 8 The three configurations under study

In all these configurations, a steady state flow is obtained. In each case, the results are compared to the reference (transparent) values, which are generated using the same gas mixture but without including any radiation effects in volume.

We present below the cross section planes and the crosslines used to display the results. The dimensionless temperature and velocity fields are plotted in the median vertical plane of the cavity ($Y = 0.5$ or $y = 0.125m$) (see figure 5). We also consider the profiles of these quantities along different crosslines in the plane $Y = 0.5$:

- Z-lines: $Z = 0.1$, $Z = 0.5$, $Z = 0.8$
- X-lines: $X = 0.2$, $X = 0.5$, $X = 0.8$

All the results presented hereafter are normalized with respect to the reference temperature $T_{ref} = \frac{T_h + T_c}{2}$, the reference length L and the reference velocity $U_{ref} = \alpha \frac{\sqrt{Ra}}{L}$

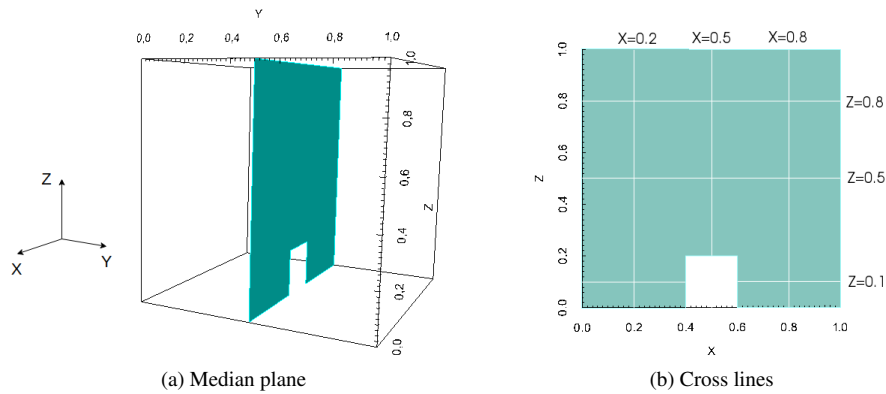


Figure 5 Median plane ($Y = 0.5$) and crosslines used for the results display

4.1 Convergence on spatial grid

Before conducting original simulations, we have analyzed the convergence of the results with respect to the spatial meshing, the angular discretization and the number of gray gases (spectral divisions) in the SLW model. We have run different tests, but we only present here those concerning natural convection case at $Ra = 5 \cdot 10^6$, $Pr = 0.71$, $T_0 = 555K$ and $\Delta T = 50K$ with black active walls and purely reflective adiabatic walls. Three uniform grids of different sizes have been considered: 80^3 , 100^3 and 120^3 .

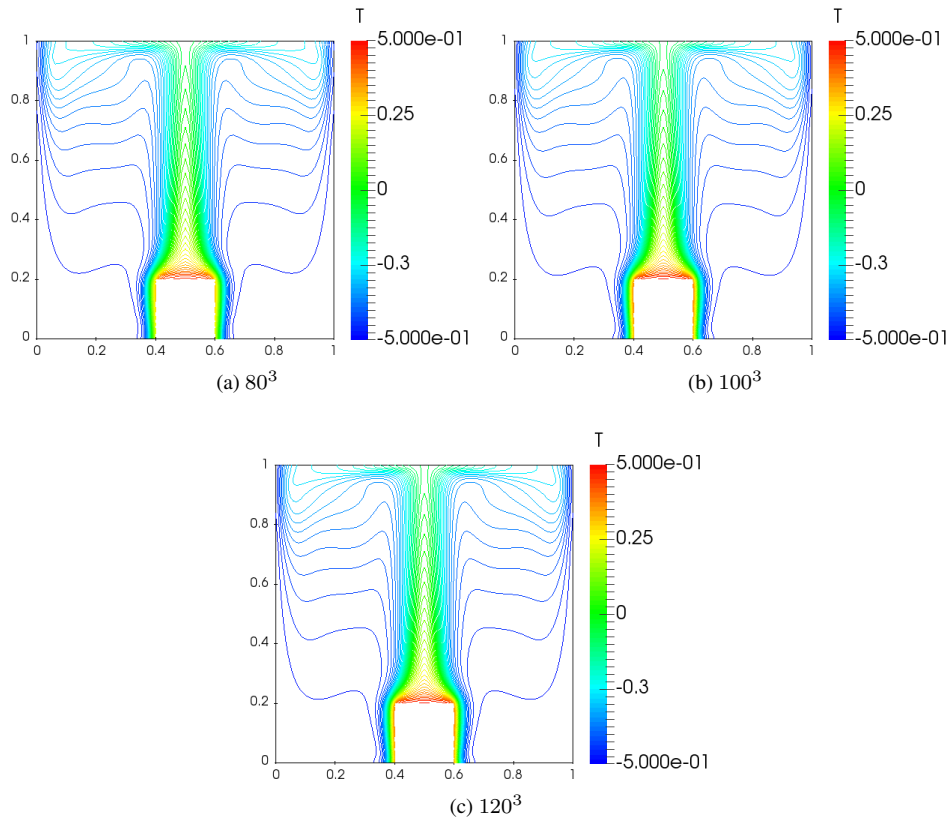


Figure 6 Temperature $\frac{T-T_{ref}}{T_h-T_c}$ distribution in the median plane ($Y = 0.5$) with different mesh sizes: transparent medium.

Mesh	u_{max} (m/s)	w_{max} (m/s)
80^3	0.191	0.339
100^3	0.191	0.342
120^3	0.191	0.342

Table 9 Maximum horizontal and vertical velocities for different mesh sizes.

Mesh	Front wall	Back wall	Left wall	Right wall
80^3	1.690	1.690	1.690	1.690
100^3	1.682	1.682	1.682	1.682
120^3	1.681	1.681	1.681	1.681

Table 10 Mean Nusselt numbers at the bounding surfaces of the enclosure.

Mesh	Front wall	Back wall	Left wall	Right wall	Top wall
80^3	38.664	38.664	38.664	38.664	14.343
100^3	38.508	38.508	38.508	38.508	14.166
120^3	38.492	38.492	38.492	38.492	14.132

Table 11 Mean Nusselt numbers at the bounding surfaces of the hot source.

From the result displayed above, we consider that the simulations are converged with respect to the spatial meshing when using a 100^3 grid. A same observation was made in configurations involving gas radiation. Therefore, we have selected this mesh for our subsequent calculations.

All the subsequent calculations have been carried out using a uniform 100^3 grid with the S_8 discrete ordinates method and a 5-gray gas SLW model.

4.2 Thermal and dynamic fields

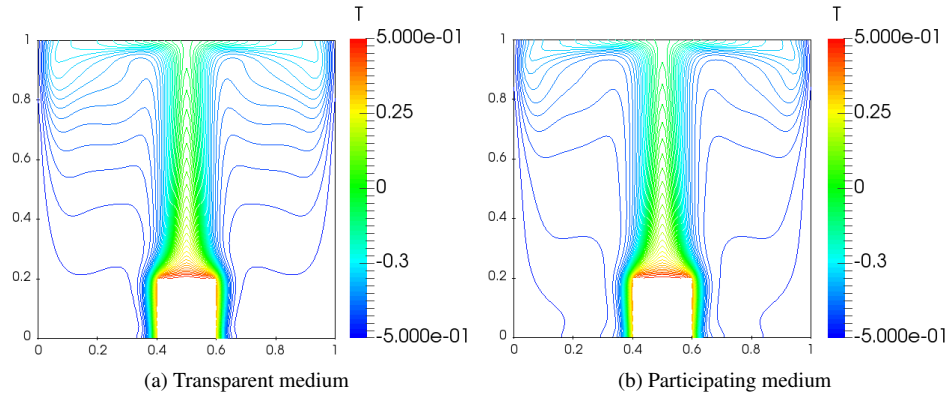


Figure 7 2D-contours of temperature $\frac{T-T_{ref}}{T_h-T_c}$ in the median plane of the cavity ($Y = 0.5$) at $x_{H_2O} = 0.05$

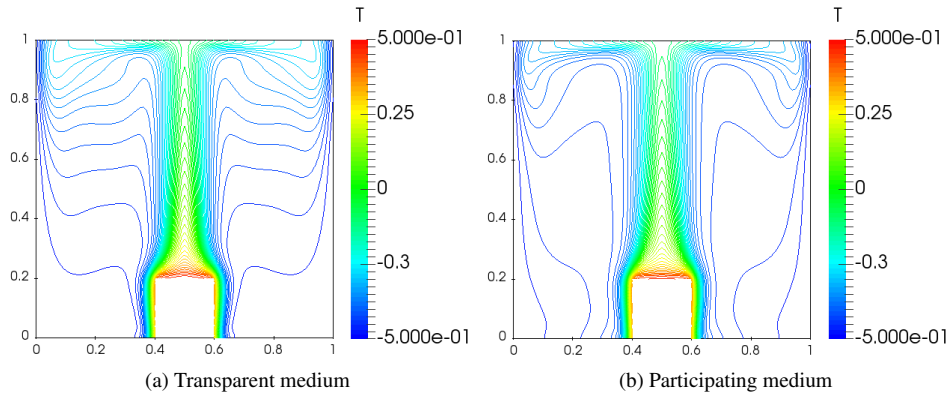


Figure 8 2D-contours of temperature $\frac{T-T_{ref}}{T_h-T_c}$ in the median plane of the cavity ($Y = 0.5$) at $x_{H_2O} = 0.10$

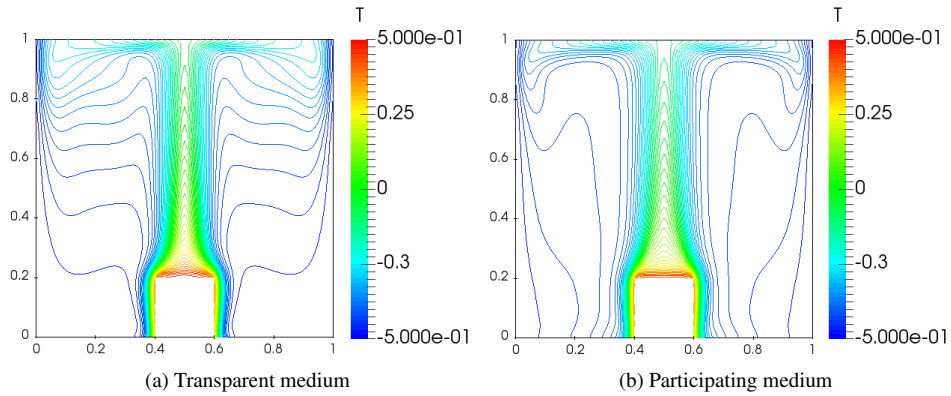


Figure 9 2D-contours of temperature $\frac{T-T_{ref}}{T_h-T_c}$ in the median plane of the cavity ($Y = 0.5$) at $x_{H_2O} = 0.20$

Figures 7, 8 and 9 display the thermal field in the median plane ($Y = 0.5$) in both cases of transparent and participating media at different concentrations of the water vapor. The most sensitive effect of radiation (at these concentrations) is a slight broadening of the temperature contours in the lower half of the cavity (Figures 7 b, 8 b, 9 b). The radiant flux coming from the hot surfaces of the obstacle heats up the medium between the heater and the vertical walls of the cavity. As a result, the nearly vertical thermal stratification in absence of radiation is broken. The air (outside the thermal plume), therefore, slightly becomes more uniform in temperature.

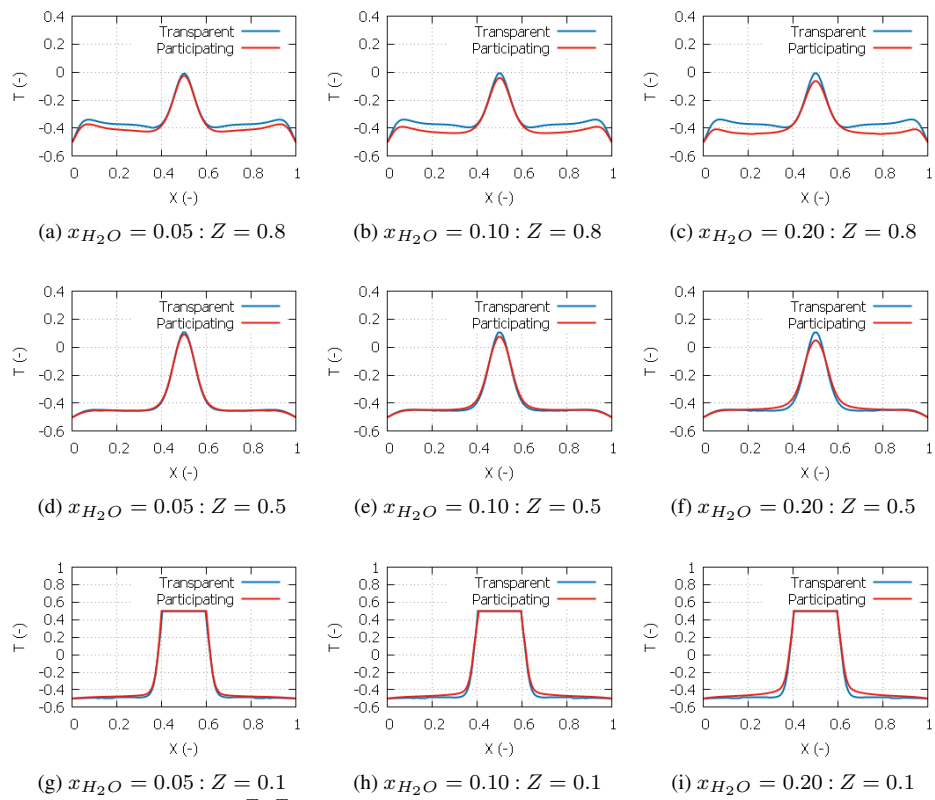


Figure 10 Temperature $\frac{T-T_{ref}}{T_h-T_c}$ profiles along different Z-cross lines in the median plane ($Y = 0.5$) at different concentrations of water vapor

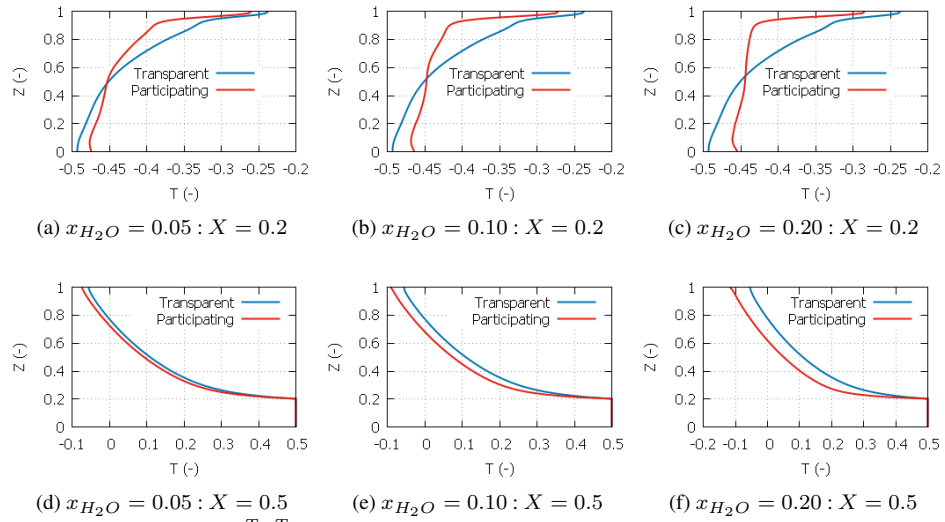


Figure 11 Temperature $\frac{T-T_{ref}}{T_h-T_c}$ profiles along different X-cross sections in the median plane ($Y = 0.5$) at different concentrations of water vapor

As a whole, radiation does not significantly change the thermal profile along the centerline ($Z = 0.5$) (see figures 10 d,e,f) and in the lower half of the cavity ($Z = 0.1$) (see figures 10 g,h,i). But at a higher position ($Z = 0.8$) (see figures 10 a,b,c), a slight decrease of temperature in the re-circulation zone between the plume and the wall boundary layer can now be observed. In this region of low convective transport, the gas radiates toward the cold surfaces and the colder parts of the fluid (it emits more than it absorbs): this results in a negative radiative source within the fluid (see figures 12 a, 13 a and 14 a).

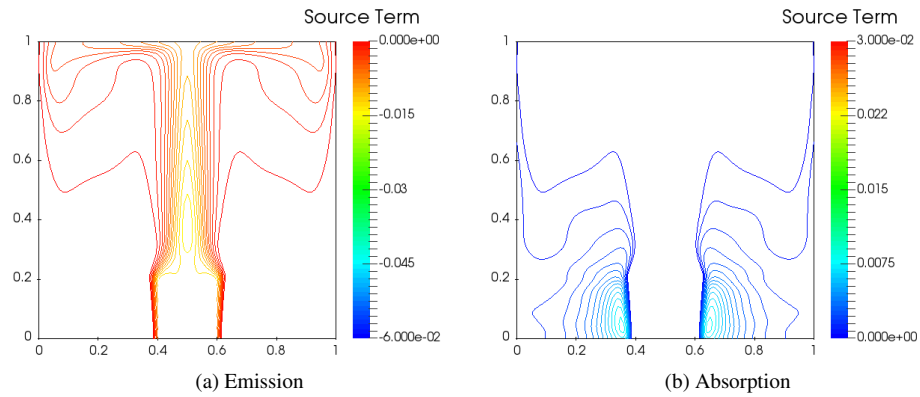


Figure 12 Distribution of radiative source term in the median plane ($Y = 0.5$) at $x_{H_2O} = 0.05$. Sources are normalized by $4\sigma T_{ref}^4/L$.

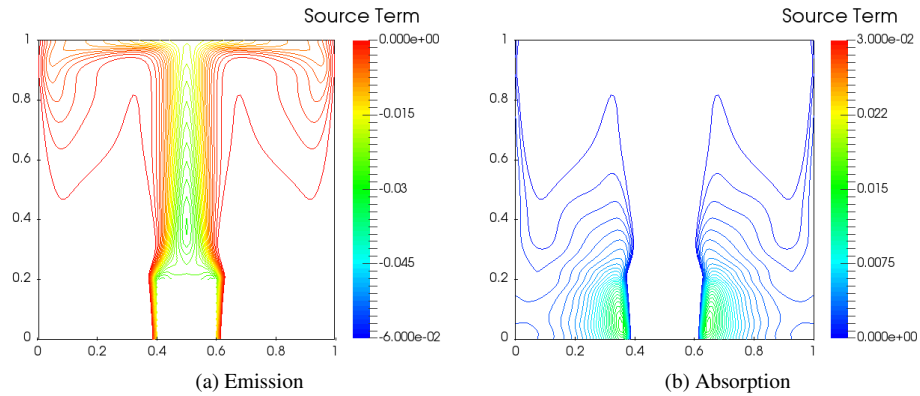


Figure 13 2D-contour of radiative source term in the median plane ($Y = 0.5$) at $x_{H_2O} = 0.10$. Sources are normalized by $4\sigma T_{ref}^4/L$.

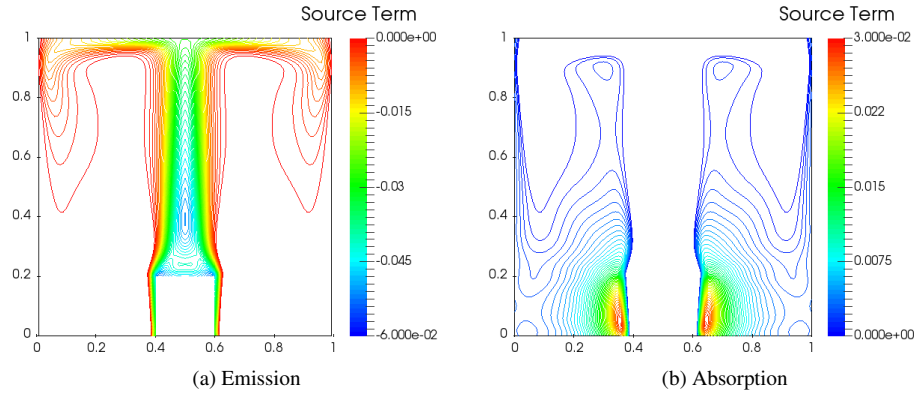


Figure 14 2D-contour of radiative source term in the median plane ($Y = 0.5$) at $x_{H_2O} = 0.20$. Sources are normalized by $4\sigma T_{ref}^4/L$.

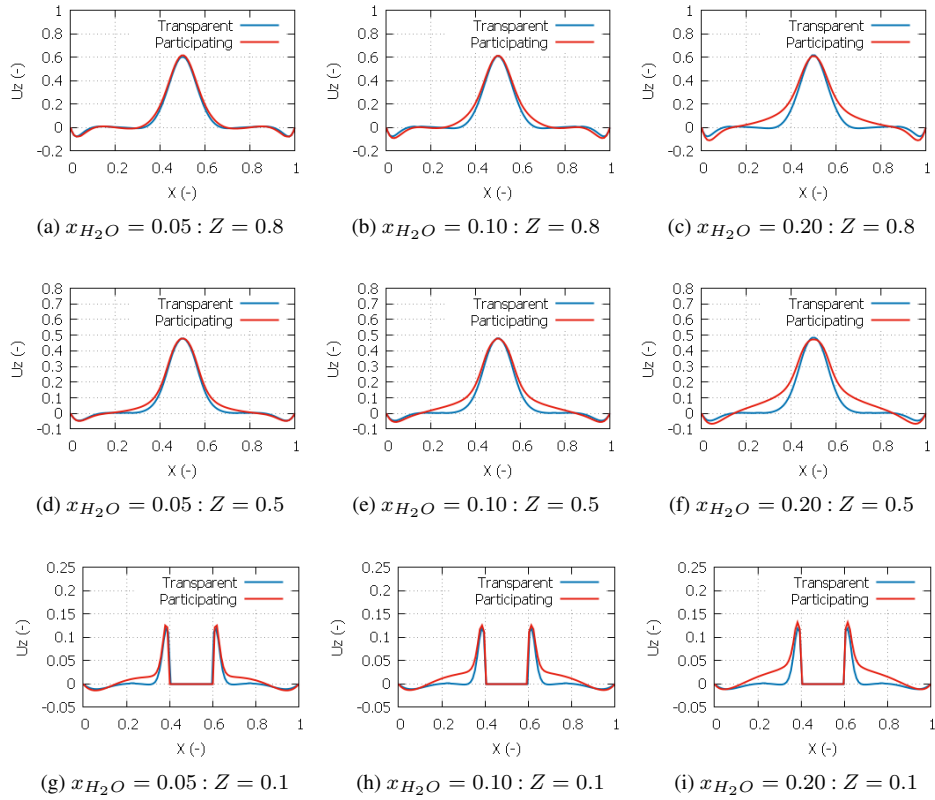
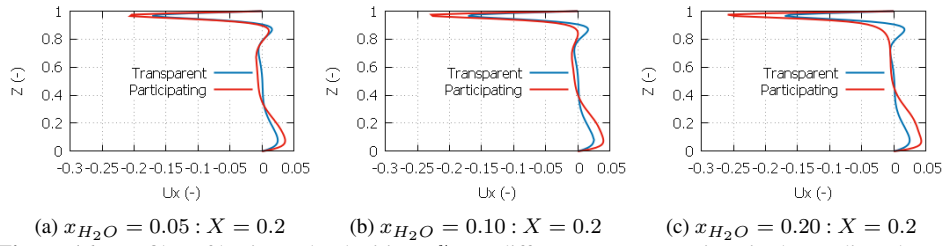


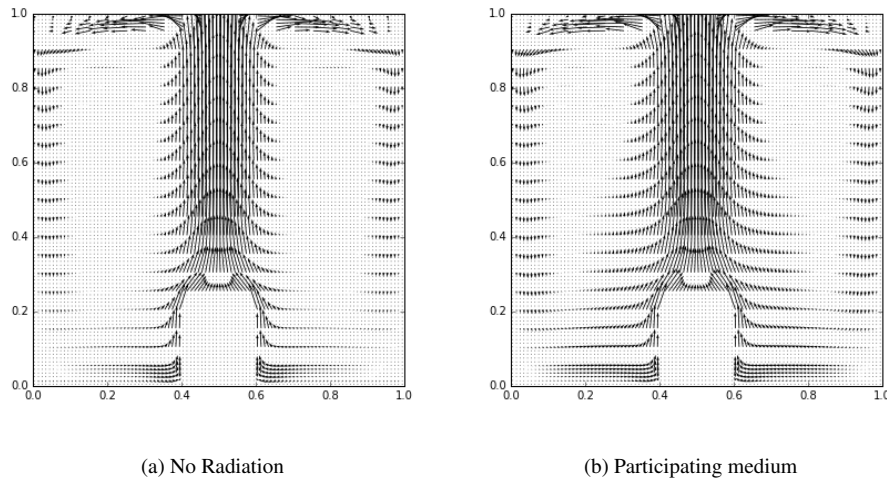
Figure 15 Profiles of vertical velocities $\frac{w}{U_{ref}}$ at different Z-cross sections in the median plane ($Y = 0.5$) at different concentrations of water vapor

Moreover, the change in the thermal field alters the buoyancy forces in the cavity. Consequently, the vertical velocities slightly increase near the lateral walls and significantly near the plume flow (see Fig 15). The two boundary layers (climbing along the obstacle, descending along the wall) now interfere and create a shear flow in this region.



(a) $x_{H_2O} = 0.05 : X = 0.2$ (b) $x_{H_2O} = 0.10 : X = 0.2$ (c) $x_{H_2O} = 0.20 : X = 0.2$
Figure 16 Profiles of horizontal velocities $\frac{u}{U_{ref}}$ at different X-cross sections in the median plane ($Y = 0.5$) at different concentrations of water vapor

Another change in the fluid motion can be found in the profiles of horizontal velocities along the vertical cross-sections, which are displayed in Fig 16 a. Compared to the transparent case, the fluid near the ceiling and the floor of the enclosure is accelerated. This is due to an increase in the mass flow driven by the plume. These alterations of the velocity field are enhanced when the medium becomes more absorbing: comparison between figures 15 b,e,h and 16 b ($x_{H_2O} = 0.10$) versus 15 c,f,i and 16 c ($x_{H_2O} = 0.20$).



(a) No Radiation (b) Participating medium
Figure 17 Vector field in the median plane ($Y = 0.5$) at $x_{H_2O} = 0.05$

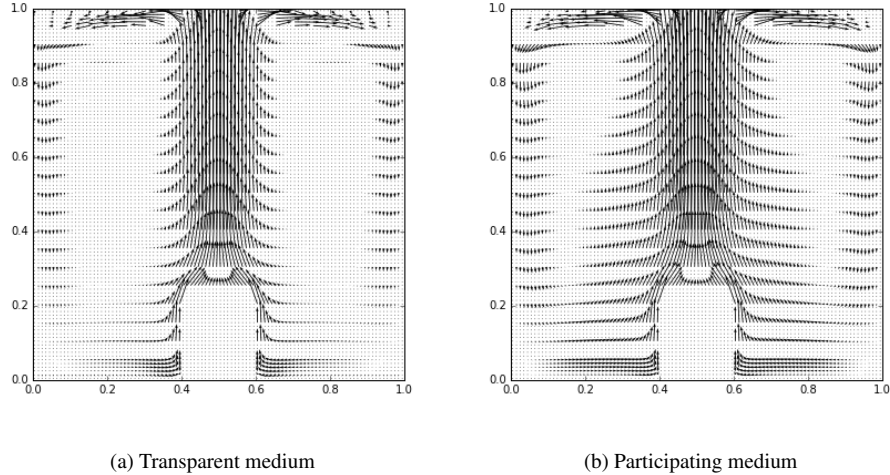


Figure 18 Vector field in the median plane ($Y = 0.5$) at $x_{H_2O} = 0.10$

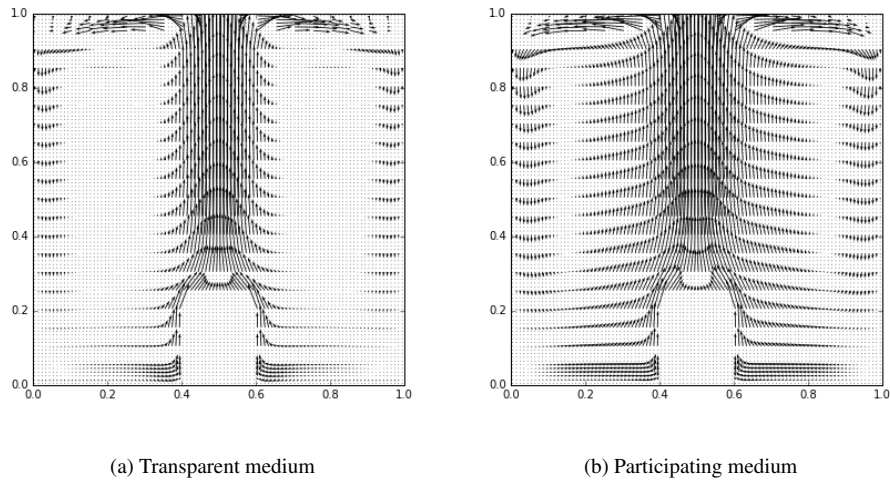


Figure 19 Vector field in the median plane ($Y = 0.5$) at $x_{H_2O} = 0.20$

Figure 17, 18 and 19 represent the velocity vectors in the mid-depth ($Y = 0.5$) plane for three concentrations of the absorbing component. They display the typical patterns explaining the formation of the plume. The fluid is accelerated along the lateral surfaces of the hot body, goes up and then combines above the top surface of the obstacle. Here, the fluid between the plume and its surroundings is pushed upward by the buoyancy force created by the temperature difference. The hot fluid, then, moves along the ceiling of the enclosure and then flows down near the cold walls. Besides, it is clearly observed that the plume broadens and the boundary layers near vertical walls get thicker when the radiation

effects are present (compared to the transparent cases).

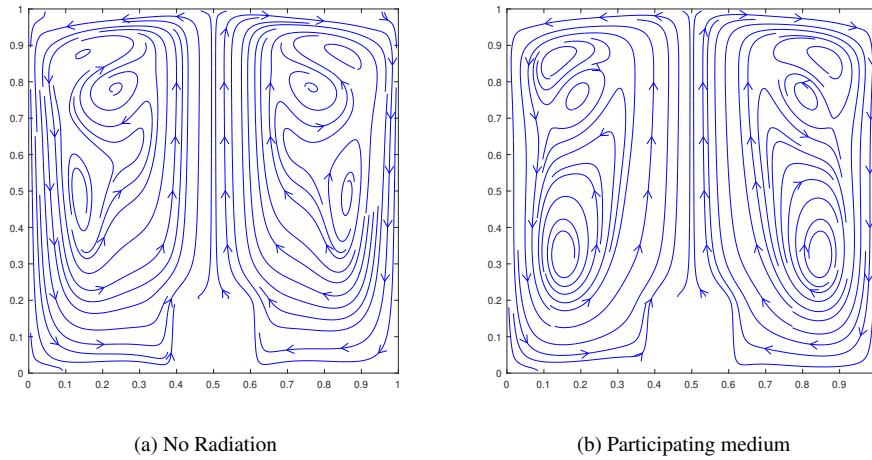


Figure 20 Flow lines in the median plane ($Y = 0.5$) at $x_{H_2O} = 0.05$

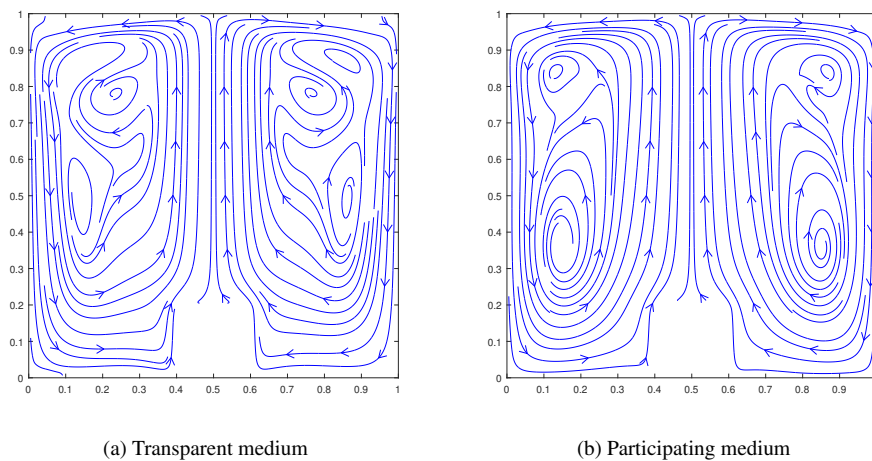


Figure 21 Flow lines in the median plane ($Y = 0.5$) at $x_{H_2O} = 0.10$

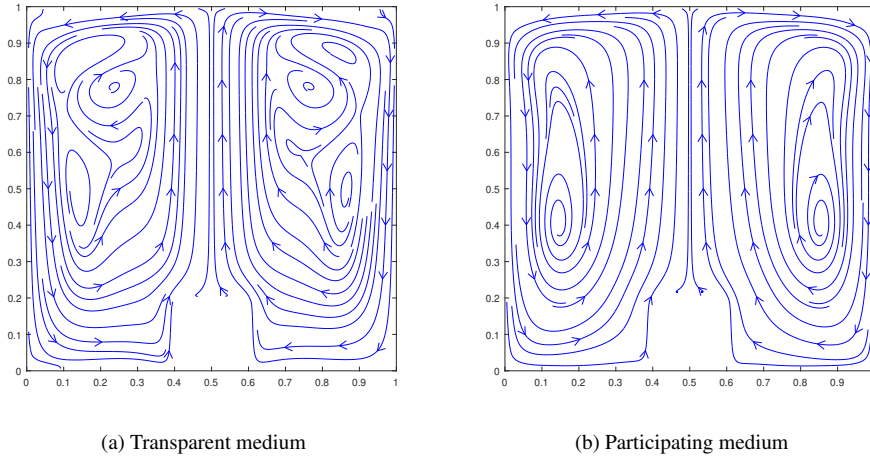


Figure 22 Flow lines in the median plane ($Y = 0.5$) at $x_{H_2O} = 0.20$

The flow line patterns show that, in the transparent case, three vortices are formed on each side of the cavity (see figure 20 a, 21 a, 22 a). They are the projections in the median plane $Y = 0.5$ of 3-D swirls, but are associated to low velocity parts of the flow. However, when the medium participates to radiation, the number of vortices decreases (see figure 20 b, 21 b, 22 b).

Similar modifications in dynamic and thermal field were reported by Billaud et al. (2017) for a differentially heated cavity: gas radiation was found to accelerate the global circulation and to set into motion some parts of the fluid that were stagnant in the transparent case.

4.3 Heat Transfer

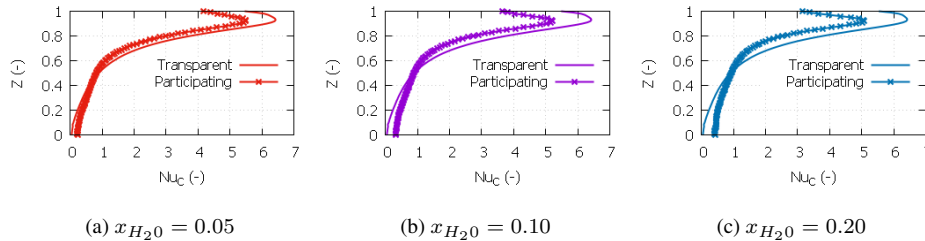


Figure 23 Local convective Nusselt number along the vertical centerline of any lateral wall of the cavity

The plots in the figure 23 clearly show that the convective Nusselt number along the centerline of any vertical wall of the enclosure is decreased close to the roof of the cavity

and increased elsewhere. The reason is that, in the upper part, the fluid was cooled down (figures 12 a, 13 a and 14 a) before reaching the lateral walls. On the other hand, in the lower part, absorption dominates over the emission (figures 12 b, 13 b and 14 b), thus, the medium is heated up and the thermal gradient is increased. However, the increased part does not compensate the decreased one. Therefore, overall, the average convective Nusselt number over the vertical wall of the enclosure is reduced (see table 12).

This decreasing trend in the local convective Nusselt number is also found when considering the vertical hot surfaces of the obstacle. This is illustrated in figure 24. The reason is that the thermal gradient is reduced when the radiation is considered. Indeed, the fluid is warmed up (by the absorption) along the floor of the enclosure before arriving at the vertical hot surfaces of the obstacle. Consequently, the average values of Nu_C displayed in table 14 are decreased when the radiation is taken into account.

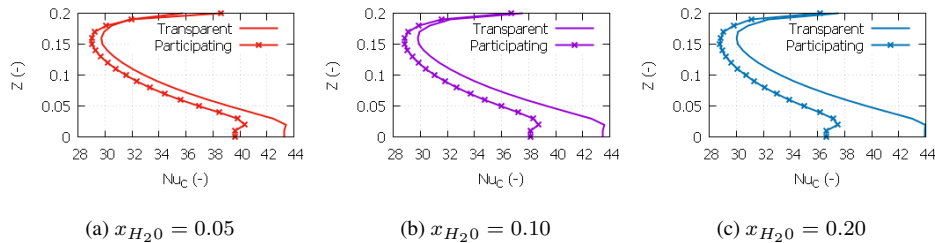


Figure 24 Local convective Nusselt number along the vertical center line of each lateral surfaces of the obstacle

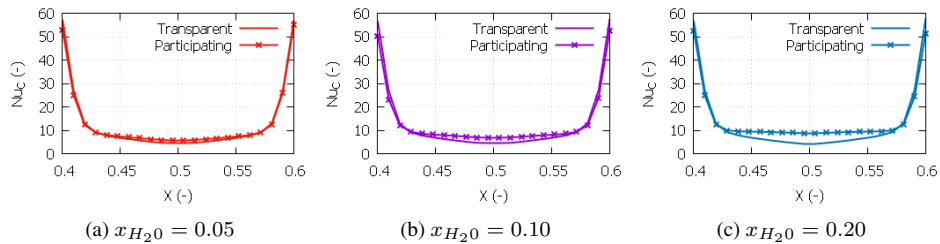


Figure 25 Local convective Nusselt number along the horizontal centerline of the obstacle top surface

However, it is observed that the convective transfer along the horizontal upper surface of the obstacle increases. When radiation is present, the fluid layer near the hot surfaces becomes cooler due to the emission (it is evidenced by the negative values of the radiative source in the figures 12, 13 and 14). Consequently, the thermal gradient in this region is enhanced, which induces the increase in local values of Nusselt number with the appearance of the radiation (figure 25). This explains the higher average convective Nusselt number obtained in table 14.

The values of average convective Nusselt number and average total Nusselt number, which

are defined as $\overline{Nu} = \frac{1}{A} \int_A Nu(\mathbf{s}) dA$, are presented in the tables below:

$x_{H_2O}(\%)$	Convective Nusselt number		Total Nusselt number	
	Transparent	Participating	Transparent	Participating
5	1.67	1.34	12.47	12.38
10	1.67	1.27	12.48	12.33
20	1.68	1.24	12.50	12.26

Table 12 Average convective and total Nusselt numbers along any vertical wall of the cavity

$x_{H_2O}(\%)$	Convective Nusselt number		Total Nusselt number	
	Transparent	Participating	Transparent	Participating
5	38.28	37.09	252.07	250.25
10	38.34	36.75	252.19	249.31
20	38.57	36.59	252.59	247.93

Table 13 Average convective and total Nusselt numbers along any vertical wall of the obstacle

$x_{H_2O}(\%)$	Convective Nusselt number		Total Nusselt number	
	Transparent	Participating	Transparent	Participating
5	14.12	14.50	239.91	238.26
10	14.17	14.90	240.03	236.92
20	14.30	15.85	240.34	234.74

Table 14 Average convective and total Nusselt numbers along the horizontal upper wall of the obstacle

Regarding the total heat transfer, the table 12, 13 and 14 reveal that, compared to the transparent cases, the average total Nusselt number along any black surfaces is decreased. This, along the vertical walls, is due to the drop off in the convective Nusselt number. In addition, the attenuation of radiative transfer by the absorbing medium also contributes to the reduction of total thermal transport, especially, when considering this quantity along the upper surfaces of the obstacle, where the convective transfer is accelerated.

5 Conclusion

The coupling of natural convection with volume radiation in a cubical cavity with a heat source located on its floor has been investigated for an *air* – *H₂O* mixture at different concentration. The radiant sources created by the gas absorption and emission in the infrared range have been computed using the discrete ordinates method and SLW model associated with the rank-correlated approach. The other conservation equations have been solved using a finite volume method implemented in the Code Saturne software. The obtained results

have been compared to the case where the medium is considered as transparent. These comparisons show that:

- Radiation tends to non-uniformly accelerate the boundary layers along the cavity and the hot inner obstacle. It also sets into motion some parts of the fluid that were stagnant in the transparent case. This results in making the plume flow and its recirculation along the walls interfere and create a shear flow.
- Radiation partly modifies the thermal gradient near the bounding surfaces of the cavity: the convective Nusselt values are increased in the upper half and decreased in the lower half. However, an inverse trend is observed at the horizontal surface of the obstacle.
- Radiation modifies the nearly vertical thermal stratification outside the plume and slightly uniformizes the medium temperature.
- The presence of radiation reduces the total thermal transfer, especially the convective part on the vertical walls and the radiative part along the upper surface of the obstacle.
- All these effects were found to increase when the medium becomes more absorbing (in the considered range of H_2O molar fractions).

References

- A Yücel, S Acharya, and M L Williams. Natural convection and radiation in a square enclosure. *Numerical Heat Transfer*, 15(2):261–278, 1989.
- Z Tan and J R Howell. Combined radiation and natural convection in a two-dimensional participating square medium. *International Journal of Heat and Mass Transfer*, 34(3):785–793, 1991.
- G Colomer, M Costa, R Consul, and A Oliva. Three-dimensional numerical simulation of convection and radiation in a differentially heated cavity using the discrete ordinates method. *International Journal of Heat and Mass Transfer*, 47(2):257–269, 2004a.
- G Colomer, R Consul, and A Oliva. Coupled radiation and natural convection: Different approaches of the slw model for a non-gray gas mixture. *Journal of Quantitative Spectroscopy and Radiative Transfer*, 107(1):30–46, 2007.
- L Soucasse, P Rivière, S Xin, P Le Quéré, and A Soufiani. Numerical study of coupled molecular gas radiation and natural convection in a differentially heated cubical cavity. *Computational Thermal Sciences: An International Journal*, 4(4), 2012.
- Y Billaud, D Saury, and D Lemonnier. Numerical investigation of coupled natural convection and radiation in a differentially heated cubic cavity filled with humid air. Effects of the cavity size. *Numerical Heat Transfer, Part A: Applications*, 72(7):495–518, 2017.
- F Hajji, A Mazgar, K Jarray, and F B Nejma. Natural convection analysis through a radiatively participating media within a rectangular enclosure. *Progress in Computational Fluid Dynamics, An International Journal*, 18(2):108–126, 2018.

- F Tetsu, M Itsuki, and U Haruo. Buoyant plume above a horizontal line heat source. *International Journal of Heat and Mass Transfer*, 16(4):755–768, 1973.
- K Urakawa, I Morioka, and M Kiyota. Swaying motion of the buoyant plume above a horizontal line heat source. In *Proc. 1st ASME-JSME Thermal Eng. Conf.*, pages 215–220, 1983.
- S Xin, M C Duluc, F Lusseyran, and P Le Quéré. Numerical simulations of natural convection around a line-source. *International Journal of Numerical Methods for Heat & Fluid Flow*, 14(7):830–850, 2004.
- R H Hernandez. Natural convection in thermal plumes emerging from a single heat source. *International Journal of Thermal Sciences*, 98:81–89, 2015.
- G V Kuznetsov and M A Sheremet. Two-dimensional problem of natural convection in a rectangular domain with local heating and heat-conducting boundaries of finite thickness. *Fluid Dynamics*, 41(6):881–890, 2006a.
- G V Kuznetsov and M A Sheremet. Conjugate heat transfer in a closed domain with a locally lumped heat-release source. *Journal of Engineering Physics and Thermophysics*, 79(1):57–64, 2006b.
- M Xu and Z Wang. The natural convection of an isolated plate in enclosures. *Progress in Computational Fluid Dynamics, An International Journal*, 8(7-8):549–553, 2008.
- M Paroncini and F Corvaro. Natural convection in a square enclosure with a hot source. *International journal of thermal sciences*, 48(9):1683–1695, 2009.
- G V Kuznetsov, V I Maksimov, and M A Sheremet. Natural convection in a closed parallelepiped with a local energy source. *Journal of Applied Mechanics and Technical Physics*, 54(4):588–595, 2013.
- B Souayah, N B Cheikh, B B Beya, and T Lili. Prediction of unsteady natural convection within a square cavity containing an obstacle at high Rayleigh number value. *International Letters of Chemistry, Physics and Astronomy*, 55:19, 2015.
- N S Gibanov and M A Sheremet. Effect of the buoyancy force on natural convection in a cubical cavity with a heat source of triangular cross-section. In *IOP Conference Series: Materials Science and Engineering*, volume 124, page 012057. IOP Publishing, 2016.
- D Iyi, R Hasan, and R Penlington. Numerical simulation of 2d turbulent natural convection of humid air in a cavity filled with solid objects. *Procedia engineering*, 56:538–543, 2013.
- A R Rahmati and A A Tahery. Numerical study of nanofluid natural convection in a square cavity with a hot obstacle using lattice boltzmann method. *Alexandria engineering journal*, 57(3):1271–1286, 2018.
- M Bouafia and O Daube. Natural convection for large temperature gradients around a square solid body within a rectangular cavity. *International Journal of Heat and Mass Transfer*, 50(17-18):3599–3615, 2007.
- H Sun, E Chénier, and G Lauriat. Effect of surface radiation on the breakdown of steady natural convection flows in a square, air-filled cavity containing a centered inner body. *Applied Thermal Engineering*, 31(6-7):1252–1262, 2011.

- S G Martyushev and M A Sheremet. Surface radiation influence on the regimes of conjugate natural convection in an enclosure with local energy source. *Thermophysics and Aeromechanics*, 20(4):417–428, 2013.
- S Saravanan and C Sivaraj. Surface radiation effect on convection in a closed enclosure driven by a discrete heater. *International Communications in Heat and Mass Transfer*, 53:34–38, 2014.
- S Patil, A K Sharma, and K Velusamy. Conjugate laminar natural convection and surface radiation in enclosures: Effects of protrusion shape and position. *International Communications in Heat and Mass Transfer*, 76:139–146, 2016.
- I Miroshnichenko, M Sheremet, and A Chamkha. Turbulent natural convection combined with surface thermal radiation in a square cavity with local heater. *International Journal of Numerical Methods for Heat & Fluid Flow*, 28(7):1698–1715, 2018.
- M K Denison and B W Webb. An absorption-line blackbody distribution function for efficient calculation of total gas radiative transfer. *Journal of Quantitative Spectroscopy and Radiative Transfer*, 50(5):499–510, 1993.
- M F Modest. *Radiative heat transfer*. Academic press, 2013.
- V Goutiere, F Liu, and A Charette. An assessment of real-gas modelling in 2d enclosures. *Journal of Quantitative Spectroscopy and Radiative Transfer*, 64(3):299–326, 2000.
- V Goutière, A Charette, and L Kiss. Comparative performance of nongray gas modeling techniques. *Numerical Heat Transfer: Part B: Fundamentals*, 41(3-4):361–381, 2002.
- M K Denison and B W Webb. k-distributions and weighted-sum-of-gray-gases-a hybrid model. In *International Heat Transfer Conference Digital Library*. Begell House Inc., 1994.
- J T Pearson, B W Webb, V P Solovjov, and J Ma. Efficient representation of the absorption line blackbody distribution function for H₂O, CO₂, and CO at variable temperature, mole fraction, and total pressure. *Journal of Quantitative Spectroscopy and Radiative Transfer*, 138:82–96, 2014.
- V P Solovjov. Tabulated data for the absorption line black body distribution function, 2014. URL <https://albdf.byu.edu/node/27>.
- V P Solovjov, F André, D Lemonnier, and B W Webb. The rank correlated slw model of gas radiation in non-uniform media. *Journal of Quantitative Spectroscopy and Radiative Transfer*, 197:26–44, 2017.
- F Archambeau, N Méchitoua, and M Sakiz. Code Saturne: A finite volume code for the computation of turbulent incompressible flows, industrial applications. *International Journal on Finite Volumes*, 1, 2004.
- R Koch and R Becker. Evaluation of quadrature schemes for the discrete ordinates method. *Journal of Quantitative Spectroscopy and Radiative Transfer*, 84(4):423–435, 2004.
- D Balsara. Fast and accurate discrete ordinates methods for multidimensional radiative transfer. part i, basic methods. *Journal of Quantitative Spectroscopy and Radiative Transfer*, 69(6):671–707, 2001.

- P Le Quéré. Accurate solutions to the square thermally driven cavity at high Rayleigh number. *Computers & Fluids*, 20(1):29–41, 1991.
- E Tric, G Labrosse, and M Betrouni. A first incursion into the 3d structure of natural convection of air in a differentially heated cubic cavity, from accurate numerical solutions. *International Journal of Heat and Mass Transfer*, 43(21):4043–4056, 2000.
- G De Vahl Davis. Natural convection of air in a square cavity: a bench mark numerical solution. *International Journal for numerical methods in fluids*, 3(3):249–264, 1983.
- G Colomer, M Costa, R Cònsul, and A Oliva. Three-dimensional numerical simulation of convection and radiation in a differentially heated cavity using the discrete ordinates method. *International Journal of Heat and Mass Transfer*, 47(2):257–269, 2004b. ISSN 00179310. doi: 10.1016/S0017-9310(03)00387-9.
- T Fusegi and J M Hyun. Laminar and transitional natural convection in an enclosure with complex and realistic conditions. *International Journal of Heat and Fluid Flow*, 15(4): 258–268, 1994.
- S Laouar-Meftah. *Modélisation de la convection naturelle de double diffusion dans un mélange de gaz absorbant et émettant le rayonnement*. PhD thesis, 2010.
- L Soucasse, P Rivière, and A Soufiani. Natural convection in a differentially heated cubical cavity under the effects of wall and molecular gas radiation at Rayleigh numbers up to 3×10^9 . *International Journal of Heat and Fluid Flow*, 61:510–530, 2016.
- S Meftah, A Ibrahim, D Lemonnier, and A Benbrik. Coupled radiation and double diffusive convection in nongray air-CO₂ and air-H₂O mixtures in cooperating situations. *Numerical Heat Transfer, Part A: Applications*, 56(1):1–19, 2009.